


Simultaneous Brillouin and piezoelectric coupling to a high-frequency bulk acoustic resonator: supplement

TAEKWAN YOON,^{1,2,†,*} DAVID MASON,^{1,2,†} VIJAY JAIN,^{1,2} YIWEN CHU,³ PRASHANTA KHAREL,^{1,2}  WILLIAM H. RENNINGER,⁴ LIAM COLLINS,⁵ LUIGI FRUNZIO,^{1,2} ROBERT J. SCHOELKOPF,^{1,2,6} AND PETER T. RAKICH^{1,2,7}

¹Department of Applied Physics and Physics, Yale University, New Haven, Connecticut 06520, USA

²Yale Quantum Institute, New Haven, Connecticut 06520, USA

³Department of Physics, ETH Zurich, 8093 Zurich, Switzerland

⁴Institute of Optics, University of Rochester, Rochester, New York 14627, USA

⁵Center for Nanophase Materials Sciences, Oak Ridge National Laboratory, Oak Ridge, Tennessee 37831, USA

⁶e-mail: robert.schoelkopf@yale.edu

⁷e-mail: peter.rakich@yale.edu

*Corresponding author: taekwan.yoon@yale.edu

[†]These authors contributed equally to this work.

This supplement published with Optica Publishing Group on 17 January 2023 by The Authors under the terms of the [Creative Commons Attribution 4.0 License](https://creativecommons.org/licenses/by/4.0/) in the format provided by the authors and unedited. Further distribution of this work must maintain attribution to the author(s) and the published article's title, journal citation, and DOI.

Supplement DOI: <https://doi.org/10.6084/m9.figshare.21666827>

Parent Article DOI: <https://doi.org/10.1364/OPTICA.474022>

Simultaneous Brillouin and piezoelectric coupling to high-frequency bulk acoustic resonator: supplemental document

1. FULL APPARATUS SETUP

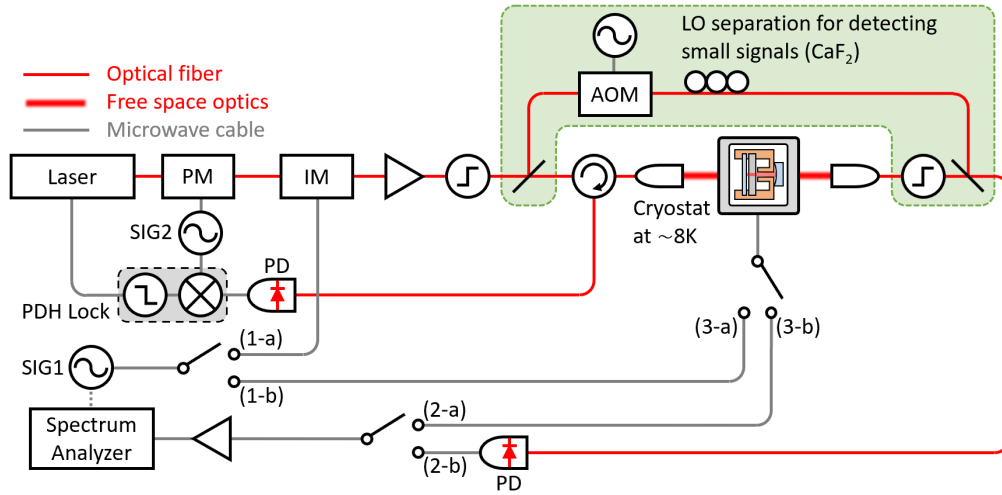


Fig. S1. Experimental apparatus PM: phase modulator, IM: intensity modulator, AOM: acousto-optic modulator, PDH: Pound-Drever-Hall, SIG: signal generator. For OMIT measurement, switch combination (1-a) and (2-b) (3-a) are used (switch 3 is irrelevant). For microwave to optical conversion, switch combination (1-b), (2-b) and (3-a) are used. For optical to microwave conversion, switch combination (1-a), (2-a) and (3-b) are used. Part of the apparatus shaded in green is not used for X-cut quartz measurement, but instead only used for CaF₂ measurement to achieve better signal-to-noise ratio for highly sensitive piezoelectricity detection.

The experimental setup is illustrated in Figure S1. The laser is locked to the optical cavity via the Pound-Drever-Hall (PDH) locking technique. The optical sidebands required for the lock are generated by the signal generator (SIG2) and the phase modulator (PM). For optomechanically-induced transparency (OMIT) measurements, a sideband is generated by an intensity modulator (IM), which is driven by a microwave signal generator (SIG1) synchronized to the readout frequency of a spectrum analyzer. Here, the main optical tone and the sideband act as the pump and probe, respectively. The beat note between the transmitted pump and probe is measured via a high speed photodetector and spectrum analyzer. The readout frequency of the spectrum analyzer can be synchronized to the frequency of the signal generator, effectively functioning as a scalar network analyzer. In the microwave-to-optical transduction configuration, the drive tone from the signal generator directly drives the microwave cavity, piezoelectrically exciting phonons from which the pump light scatters to achieve electro-optical conversion. For optical-to-microwave transduction, the optical probe is generated from the pump using the intensity modulator. However, instead of measuring the optical response of the probe (as in OMIT), the spectrum analyzer directly reads the signal leaving the microwave cavity.

For the OMIT/transduction measurements performed on quartz, the transmitted pump serves as a local oscillator (LO) for high-frequency heterodyne detection of the signal sideband. In this configuration, it is not easy to attenuate the LO power (e.g. to avoid detector saturation) without

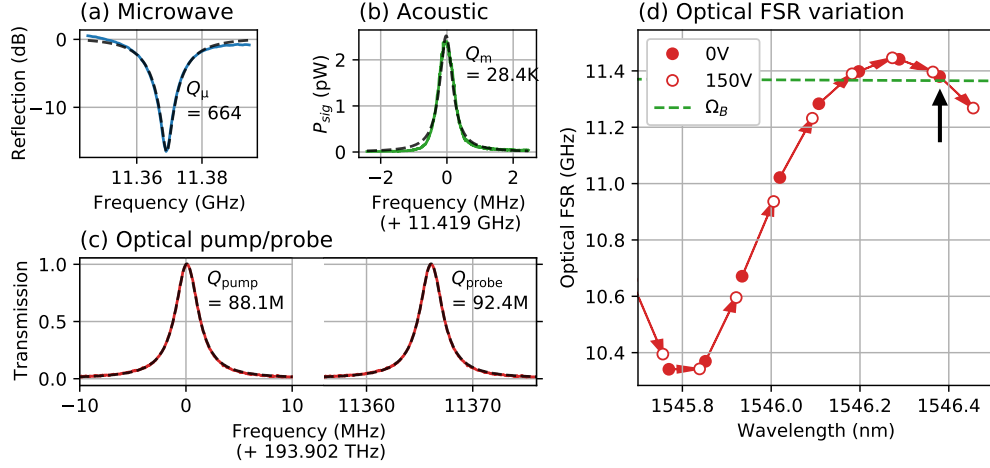


Fig. S2. Cavity loss and tunability characterization (a) Microwave, (b) acoustic, and (c) optical cavity spectrum with corresponding Q-factor. (d) Illustration of optical cavity mode-spacing tunability. Red datapoints show varying FSR at different optical wavelength whereas red arrow shows the tuning range we could achieve with a piezo actuator controlling the optical cavity length. Black arrow indicates one of the crossing points between optical cavity mode-spacing and Brillouin frequency where we chose to operate at.

also attenuating the signal. Therefore, for enhanced sensitivity in the CaF_2 measurements, we modify the circuit (green shaded box of Figure S1), filtering out the transmitted pump and using a separate, controllable LO derived from the original laser. We also shift the frequency of this new LO using an Acousto-Optic Modulator (AOM) to avoid microwave crosstalk in the detection channel. The spectrum analyzer frequency can be offset accordingly to accommodate this shift between drive frequency and heterodyne frequency, resulting in a unique signal frequency to avoid any potential microwave crosstalk. Using this separate-path LO can introduce low-frequency phase noise ($< 1\text{kHz}$) in the heterodyne beat note, which does not impact our measurements.

2. INDIVIDUAL CAVITY CHARACTERIZATION

In section 3 of the manuscript, we list the loss rates and the Q factors (finesse for optical cavity) of optical, acoustic, and microwave cavities ($\kappa_{\text{opt}}/2\pi = 2.2\text{MHz}$, $\mathcal{F} = 5170$, $\Gamma/2\pi \approx 500\text{kHz}$, $Q_m = 22800$, $\kappa_\mu/2\pi = 17.1\text{MHz}$, $Q_\mu = 664$) used for x-cut quartz demonstration of piezo-Brillouin spectroscopy. Figure S2(a-c) are the cavity spectroscopy data with fits for x-cut quartz.

Figure S2(a) shows a normalized reflection measurement of the microwave resonator, from which we find $\kappa_{\mu,i}/2\pi = 9.79\text{MHz}$ ($Q_{\mu,i} = 1160$), $\kappa_{\mu,c}/2\pi = 7.33\text{MHz}$ ($Q_{\mu,c} = 1550$), giving a total of $\kappa_\mu/2\pi = 17.1\text{MHz}$ ($Q_\mu = 662$). We use a coaxial stub cavity as the microwave cavity. The body of cavity is made out of OFHC copper, while a brass screw with a center through-hole is used as the center pin in order to achieve high tunability in resonance frequency. The seam loss between the copper body and the brass center pin results in a rather modest microwave Q factor in the current design. Figure S2(c) shows (normalized) transmission measurements for the two optical cavity modes used as pump and signal mode. We use optical sidebands to calibrate a linear frequency sweep over the modes, from which we can extract their linewidths. A broader, calibrated wavelength scan is used to identify the mode spacing. Due to the dielectric interface within the cavity, it is possible to have asymmetric cavity loss rates through the two mirrors, even though they have nominally identical reflectivities. Measurements of the resonant transmission and reflection are used to extract the relative loss rates through each mirror, as well as the internal loss. For both pump/probe modes of the optical cavity, we observe coupling rates of $\kappa_{\text{opt},c1}/2\pi \approx 0.7\text{MHz}$ and $\kappa_{\text{opt},c2}/2\pi \approx 1.2\text{MHz}$, giving an internal loss rate of $\kappa_{\text{opt},i}/2\pi \approx 0.3\text{MHz}$ and combined loss rate of $\kappa_{\text{opt}}/2\pi \approx 2.2\text{MHz}$. Figure S2(b) presents characterization data for an acoustic mode in x-cut quartz. Specifically, we present single-pass piezo-Brillouin spectroscopy data (for which the optomechanical cooperativity is small, ensuring that we measure the bare mechanical linewidth in the absence of any optomechanical backaction).

Optical cavity FSR tunability

The Fabry-Perot optical cavity used in our platform consists of two dielectric mirrors with 99.9% reflectivity and a dielectric substrate (quartz or CaF_2) in the middle. The non-zero reflection of optical mode at the boundary of the dielectric media produces an intrinsic modulation of optical mode spacing. For the cavity geometry used here (11 mm vacuum, 0.5 mm quartz), we find modulation by ± 0.5 GHz around a mean spacing of 10.9 GHz. This variation allows us to find a mode spacing that approximately matches the Brillouin frequency. In the experiments here, we pump the lower-frequency mode, using the upper-frequency mode to resonantly match the anti-Stokes sideband. Since the mode spacing variation is larger than the optical cavity linewidth, the other (Stokes) process is strongly suppressed.

In situ fine-tuning of optical cavity mode spacing at cryogenic temperatures is achieved through the use of a piezo-actuator that allows translation of one mirror position. With this, we can match the optical mode spacing to the acoustic mode within the both optical and acoustic linewidths ($\Delta_{\text{opt}} \approx \Omega_m$).

The frequency tuning range is shown in Figure S2(d), where we clearly see greater than 10% (> 1 GHz) intrinsic variation, plus fine-tuning via the piezo-actuator voltage (0V \sim 150V) to match the optical mode spacing (red arrow) with the acoustic mode (green dashed line). In our experiment, we operate at optical wavelength of ~ 1546.4 nm, indicated in back arrow in the figure.

3. COUPLING RATE CHARACTERIZATIONS

A. Electromechanical coupling rate

The electromechanical interaction Hamiltonian can be expressed as a product between piezo-induced stress field ($\sigma(\vec{r}) = \vec{\bar{c}} : \vec{\bar{d}} \cdot E(\vec{r})$) and strain field in the substrate ($s(\vec{r})$), given as $H_{\text{int}} = \int \sigma(\vec{r})s(\vec{r})dV$, where $\vec{\bar{c}}$ is the stiffness tensor, $\vec{\bar{d}}$ is the piezoelectric tensor, and $:$ is tensor product. In our system, the coupling occurs predominantly between the z-directional electric and strain field due to the microwave cavity design and material properties. Thus we consider longitudinal strain fields ($s(\vec{r}) = S_z(\vec{r})$) interacting with an electric field along the z-axis ($\sigma(\vec{r}) = c_{33}d_{33}E_z(\vec{r})$), resulting in $H_{\text{int}} = c_{33}d_{33} \int E_z(\vec{r})S_z(\vec{r})dV$. Quantizing the electric ($E_z(\vec{r}) = \vec{E}_0(\vec{r})(a + a^\dagger)$) and strain fields ($S_z(\vec{r}) = \vec{S}_0(\vec{r})(b + b^\dagger)$), the interaction Hamiltonian becomes

$$\hbar g_{\text{em}} = c_{33}d_{33} \int_{\text{pz}} \vec{E}_0(\vec{r})\vec{S}_0(\vec{r})dV, \quad (\text{S1})$$

where $\int_{\text{pz}} dV$ is a volume integral across the piezoelectric substrate.

Acoustic strain field is assumed to be a standing wave in longitudinal direction and a Gaussian shape in transverse direction with mode waist proportional to the probing optical mode waist[1] ($r_m = r_{\text{opt}}/\sqrt{2}$, where r_m is the acoustic mode waist and r_{opt} is the optical mode waist), resulting in an expression

$$\vec{S}_0(\vec{r}) = s_0 e^{-\frac{r^2}{r_m^2}} \sin\left(\frac{2\pi z}{\lambda_m}\right) \hat{z}. \quad (\text{S2})$$

λ_m is the acoustic wavelength, $s_0 = \sqrt{\frac{2\hbar\Omega}{c_{33}L_m A_m}}$ is the zero point strain, L_m is the crystal thickness, and A_m is the acoustic mode area.

The microwave mode is concentrated around the central pin of a coaxial microwave cavity, resulting in a spherical mode shape with a radius of ~ 3 mm. Meanwhile, mode waist (radius) of the cylindrical acoustic mode is ~ 50 μm , which is substantially smaller than that of the microwave mode. Moreover, the thickness of the crystalline substrate varies between 0.5 mm and 1 mm, which is also smaller compared to the microwave mode waist. As a result, the electric field parallel to the phonon propagation (\hat{z} -direction) within the microwave/acoustic mode overlap volume can be assumed to be uniform,

$$\vec{E}_0(\vec{r}) = E_0 \hat{z}, \quad (\text{S3})$$

where $E_0 = \sqrt{\frac{\hbar\Omega}{2\epsilon_0\epsilon_r V_\mu}}$ is the uniform zero-point electric field strength within the overlapping mode volume. We can obtain Electric field of the system through HFSS (3D high frequency simulation software). It is convenient to output the electric field values of the microwave mode when the E-field is at its maximum and H-field is zero for a stored energy of $\hbar\Omega$. E-field value

from the simulation ($\bar{E}_{\text{sim}}(\bar{r})$) follows, $\hbar\Omega = \frac{\epsilon_0\epsilon_r}{2} \int dV |\bar{E}_{\text{sim}}(\bar{r})|^2$. Within the microwave/acoustic mode overlap volume, we see uniform simulated electric field ($\bar{E}_{\text{sim}}(\bar{r}) = E_{\text{sim}}\hat{z}$). In terms of zero-point field, simulated field amplitude can be expressed as, $E_{\text{sim}} = 2E_0$.

Combining equations (S1), (S3) and (S2), we obtain the electromechanical coupling rate,

$$\begin{aligned} g_{\text{em}} &= \frac{1}{\hbar} c_{33} d_{33} s_0 E_0 \int_{\text{pz}} e^{-\frac{r^2}{r_m^2}} \sin\left(\frac{2\pi z}{\lambda_m}\right) dV \\ &= d_{33} E_{\text{sim}} \frac{\lambda_m}{\pi} \sqrt{\frac{\Omega c_{33} A_m}{2\hbar L_m}} \sin^2\left(\frac{\pi t_{\text{pz}}}{\lambda_m}\right), \end{aligned} \quad (\text{S4})$$

where t_{pz} is the piezoelectric substrate thickness.

There are three distinct cases of piezoelectric coupling that one can consider. Firstly, piezoelectricity can be distributed evenly throughout the entire bulk of the acoustic substrate. In this case, acoustic modes with an even longitudinal index ($t_{\text{pz}} = n\frac{\lambda_m}{2}$ with even n) will have zero coupling rate ($\sin^2\left(\frac{\pi t_{\text{pz}}}{\lambda_m}\right) = 0$), while the odd index modes ($t_{\text{pz}} = n\frac{\lambda_m}{2}$ with odd n) will have maximal coupling ($\sin^2\left(\frac{\pi t_{\text{pz}}}{\lambda_m}\right) = 1$). Secondly, substrates may have surface piezoelectricity on one side of the substrate. In this case, piezoelectricity is concentrated within a thin surface layer on one surface with thickness t_{pz} ($t_{\text{pz}} \ll \lambda_m$), while the bulk remains non-piezoelectric, resulting in a simplification of the sin term in the coupling rate expression as $\sin^2\left(\frac{\pi t_{\text{pz}}}{\lambda_m}\right) = \left(\frac{\pi t_{\text{pz}}}{\lambda_m}\right)^2$. Lastly, there is the case for surface piezoelectricity on both sides of the substrate. Here, the modulation of zero and non-zero coupling rate for even and odd indexed acoustic modes appears as in the bulk piezoelectricity case, while the non-zero coupling rate is proportional to t_{pz}^2 as in the single-sided surface piezoelectricity case. With these observations in mind, we examine our experimental results in Section 5 (on X-cut quartz) and Section 7 (on CaF_2) of the supplement.

Another aspect of g_{em} is that it has a factor of $1/\sqrt{L_m}$. Although we are integrating along the full length of the substrate, the sin term results in values equivalent to integrating along an effective piezoelectric thickness of $t_{\text{pz}} < \lambda_m/2$. Hence the factor, $1/\sqrt{L_m}$, from strain normalization term remains throughout the expression of g_{em} . Such dependency of g_{em} in substrate thickness suggests that using thinner substrate is advantageous in achieving larger g_{em} , which we will later discuss the supplement.

B. Optomechanical coupling rate

Here, we derive the Brillouin optomechanical coupling rate, closely following prior studies[1, 2]. Specifically, we consider phase-matched photoelastic coupling between optical Fabry Perot modes and longitudinal bulk acoustic resonances. The electric field profile of the j -th optical cavity mode is given by

$$E_j(r, z, t) = E_{j,0} e^{-r^2/r_{\text{opt}}^2} \sin(k_j z) (a_j(t) + a_j^\dagger(t)) \quad (\text{S5})$$

where $E_{j,0} = \sqrt{\frac{2\hbar\omega_j}{\epsilon_0\epsilon_r A_{\text{opt}} L_{\text{opt}}}}$ is the zero-point field, ω_j is the j -th optical cavity mode frequency, A_{opt} (L_{opt}) is optical mode area (optical cavity length), ϵ_0 (ϵ_r) is vacuum (relative) permittivity, k_j is j -th optical wavevector, and a_j is the annihilation operator for j -th optical mode. Note that for simplicity, this model neglects modifications of the optical field due to the combined vacuum/dielectric composition of the cavity. Full modelling of the optical mode profile, in the presence of this dielectric interface, is possible through use of a transfer matrix model [1]. For the acoustic modes, we write the displacement of the i -th longitudinal mode as

$$U_z(r, z, t) = U_{i,0} e^{-r^2/r_m^2} \cos(q_i z) (b_i(t) + b_i^\dagger(t)), \quad (\text{S6})$$

where $U_{i,0} = \sqrt{\frac{2\hbar}{\rho\Omega_m A_m L_m}}$ is the zero-point displacement, ρ is crystal density, q_i is i -th acoustic wavevector, and b_i is the annihilation operator for i -th acoustic mode. Since we are using a plano-plano (as opposed to plano-convex) crystal for the acoustic resonator, our acoustic mode waist is not independently determined by the crystal geometry, but rather defined by the optical mode waist. Specifically, $r_m = r_{\text{opt}}/\sqrt{2}$.

The photoelastic interaction Hamiltonian is given by

$$H_{\text{int}} = \frac{1}{2} \epsilon_0 \epsilon_r^2 p_{13} \int \left(\frac{\partial U}{\partial z} \right) E_{\text{opt}}^2 dV, \quad (\text{S7})$$

where p_{13} is the relevant photoelastic constant. In anticipation of the phase-matching requirement, we will consider intermodal coupling involving the j and $j + 1$ optical modes with wavevectors/frequencies which satisfy $k_{j+1} + k_j = q_i$ and $\Omega_m = \omega_{j+1} - \omega_j$. Since $\omega_j \approx \omega_{j+1}$, this yields the Brillouin phase-matching condition from the main text ($q_i = 2n\omega_j/c$). Plugging in the appropriate mode definitions and making the rotating wave approximation, the interaction Hamiltonian is

$$H_{\text{int}} = \frac{1}{2}\epsilon_0\epsilon_r^2 p_{13} \int dV q_i U_{i,0} E_{j+1,0} E_{j,0} e^{-\frac{r^2}{r_m^2}} e^{-\frac{r^2}{r_{\text{opt}}^2}} e^{-\frac{r^2}{r_{\text{opt}}^2}} \sin(q_i z) \sin(k_{j+1} z) \sin(k_j z) (a_{j+1}^\dagger a_j b_i + H.C.), \quad (\text{S8})$$

Note that here we have assumed the crystal begins precisely at $z = 0$ (i.e. coincident with the mirror). In reality, the longitudinal component of this overlap integral will depend sensitively on the position of the acoustic standing wave within the optical standing wave. As shown in [1], the approach we take here offers a good estimate of the *maximum* possible coupling rate. Experimental values may differ by up to a factor of 2, based on this exact longitudinal overlap. This approximation, as well as the choice to neglect optical field redistribution due to the dielectric interface, constitute the main sources of uncertainty in predicting the cavity optomechanical coupling rate.

The interaction Hamiltonian can be alternatively written in terms of the single-photon coupling rate, $g_{\text{om},0}$, as following,

$$H_{\text{int}} = \hbar g_{\text{om},0} (a_{j+1}^\dagger a_j b_i + H.C.). \quad (\text{S9})$$

Combining Equation S8 and S9, we obtain the single-photon coupling rate in the presence of an optical cavity,

$$g_{\text{om},0} = \frac{\omega_j^2 n^3 p_{13}}{8c} \sqrt{\frac{2\hbar}{\Omega_m \rho A_m L_m}} \frac{L_m}{L_{\text{opt}}}. \quad (\text{S10})$$

The x-cut quartz OMIT measurements from Figure 2 of the main text offer a direct measurement of the cavity-enhanced coupling rate. Using cavity parameters to calculate the intracavity power, we can infer an experimental value of $g_{\text{om},0} = 5.28$ Hz which closely agrees with the analytical value of $g_{\text{om},0} = 5.89$ Hz from Equation S10. For all data presented, experimental value is used unless specified.

Optical cavity-enhanced g_{om} is obtained by linearizing around a strong pump ($H_{\text{int}} = \hbar g_{\text{om},0} a_{j+1}^\dagger a_j b_i \approx \hbar \sqrt{N_p} g_{\text{om},0} a_{j+1}^\dagger b_i = \hbar g_{\text{om}} a_{j+1}^\dagger b_i$), giving the expression, $g_{\text{om}} = \sqrt{N_p} g_{\text{om},0}$, where N_p is the inter-cavity pump photon number. In our case, the maximum cavity-enhanced g_{om} achievable in our system is $g_{\text{om}} = 1.4$ MHz from OMIT ($N_p \sim 7 \times 10^{10}$ for 112 mW of pump power)

C. Optomechanical coupling rate and cooperativity in single-pass configuration

In single-pass configuration without an optical cavity, we can consider an optical cavity with $L_{\text{opt}} = L_m$ where the boundaries are defined by the acoustic crystal surfaces. This removes the filling-factor term ($\frac{L_m}{L_{\text{opt}}} = 1$) from Equation S10 in describing the single-pass single-photon

optomechanical coupling rate, resulting in an expression, $g'_{\text{om},0} = \frac{\omega_j^2 n^3 p_{13}}{8c} \sqrt{\frac{2\hbar}{\Omega_m \rho A_m L_m}}$.

Free-space cooperativity of an optomechanical system with an acoustic cavity but without an optical cavity is defined in reference [2] as

$$C_{\text{om},0}^{\text{sp}} = \frac{P_p}{\hbar \omega_p} \frac{L_m}{v_{g,p}} \frac{L_m}{v_{g,s}} \frac{g_{\text{om},0}^2}{\Gamma}, \quad (\text{S11})$$

where P_p is the pump power, ω_p is the optical pump wavelength, $v_{g,p}$ ($v_{g,s}$) is the group velocity of the pump (signal) light and Γ is the acoustic loss rate. Introducing group delay ($\tau = L_m n/c$), and inter cavity photon number ($N_p = P_p L_m / (\hbar \omega_p v_{g,p})$), the single-pass cooperativity can be re-written in a simpler form, $C_{\text{om}}^{\text{sp}} = \frac{g_{\text{om}}^2}{\Gamma \tau}$.

4. OPTICAL CAVITY ENHANCEMENT OF SIGNAL

Here, we consider the specific configuration in which one seeks to measure an optical sideband scattered from a (piezoelectrically-driven) phonon population. In particular, we analyze the optical power in the scattered sideband on both single-pass and optical cavity configuration, to illustrate the benefit of the optical cavity.

A. Signal without optical cavity enhancement

In the absence of an optical cavity, a strong pump can still scatter off phonons to generate a Brillouin sideband. Following reference [2], the optical power in this sideband can be written as

$$P'_{\text{sig}} = \left(\frac{g'_{\text{om},0} L_m}{v_o} \right)^2 P_p n_m. \quad (\text{S12})$$

B. Signal with optical cavity enhancement

In the case where we do consider an optical cavity, it becomes natural to describe the optomechanical interaction through coupled equations of motion for the pump and signal fields. In the rotating frame, this can be written as,

$$\begin{aligned} \dot{a}_s &= i\sqrt{N_p} g_{\text{om},0} b - \frac{\kappa_{\text{opt}}}{2} a_s \\ \dot{a}_p &= -\frac{\kappa_{\text{opt}}}{2} a_p + \sqrt{\kappa_{\text{opt},c}} a_{\text{in}}, \end{aligned} \quad (\text{S13})$$

where a_{in} is the external pump drive field ($P_p / \hbar \omega_p = \langle a_{\text{in}}^\dagger a_{\text{in}} \rangle$), a_s (a_p) is annihilation operator for the signal (pump) mode, b is annihilation operator for phonons, κ_{opt} ($\kappa_{\text{opt},c}$) is optical cavity loss (coupling) rate. A more extensive Hamiltonian approach will be taken in the later state space model section of the supplement. Certain simplifications are made in this section ($\Delta_o = 0, g_{\text{eo}} = 0$).

In steady state, we obtain

$$\begin{aligned} i\sqrt{N_p} g_{\text{om},0} b &= \frac{\kappa_{\text{opt}}}{2} a_s \\ \frac{\kappa_{\text{opt}}}{2} a_p &= \sqrt{\kappa_{\text{opt},c}} a_{\text{in}}. \end{aligned} \quad (\text{S14})$$

Inter-cavity pump photon number can then be written as

$$\left(\frac{\kappa_{\text{opt}}}{2} \right)^2 N_p = \kappa_{\text{opt},c} \langle a_{\text{in}}^\dagger a_{\text{in}} \rangle. \quad (\text{S15})$$

From input-output formalism, Equation S14, and Equation S15, outgoing scattered signal field (a_{out}) is

$$\begin{aligned} a_{\text{out}} &= \sqrt{\kappa_{\text{opt},c}} a_s \\ &= \left(\frac{\sqrt{\kappa_{\text{opt},c}}}{\kappa_{\text{opt}}} \right)^2 (4i g_{\text{om},0}) \sqrt{\langle a_{\text{in}}^\dagger a_{\text{in}} \rangle} b, \end{aligned} \quad (\text{S16})$$

and the corresponding scattered signal power is

$$P_{\text{sig}} = 16 \left(\frac{\kappa_{\text{opt},c}}{\kappa_{\text{opt}}^2} \right)^2 g_{\text{om},0}^2 P_p n_m. \quad (\text{S17})$$

C. Resonant enhancement of signal

Comparing Equation S12 and Equation S17, we get a ratio of

$$\begin{aligned} \frac{P_{\text{sig}}}{P'_{\text{sig}}} &= \frac{16 \left(\frac{\kappa_{\text{opt},c}}{\kappa_{\text{opt}}^2} \right)^2 g_{\text{om},0}^2 P_p n_m}{\left(\frac{g'_{\text{om},0} L_m}{v_o} \right)^2 P_p n_m} \\ &= \frac{16}{\pi^2} \eta_{\text{opt}}^2 \mathcal{F}^2. \end{aligned} \quad (\text{S18})$$

Assuming everything was kept constant, we expect $16\mathcal{F}^2$ improvement in signal power by introducing an optical cavity with with a finesse, \mathcal{F} .

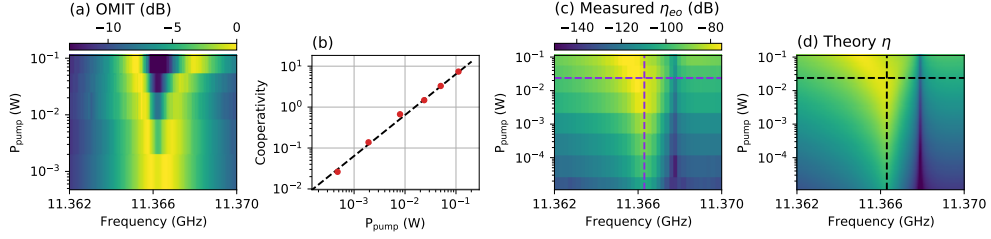


Fig. S3. Full OMIT and transduction spectrum for x-cut quartz (a) colorplot of OMIT spectrum on x-cut quartz with varying optical pump power. Clear splitting of the optomechanical response indicates strong coupling. (b) Linear relation between cooperativity fitted from data in (a) and optical pump power. (c) Measured microwave-to-optical conversion at varying pump power. Shifting of transduction peak is clearly visible, indicating we are reaching $C_{om} > 1$. EO effect induced dip on the right side of the transduction peak is also visible. Dashed line in purple is the cross section along which Figure 3 in the main text is plotted. (d) Expected transduction spectrum closely following the measurement. Color scale is set to be identical to (c). Dashed line in black is the cross section along which Figure 3 in the main text is plotted.

5. TRANSDUCTION SPECTRUM

A. X-cut quartz: transduction

Beyond what is presented in Figure 2 and Figure 3 in the main text, additional characterization can be made for x-cut quartz, as shown in Figure S3. We performed a series of OMIT measurement at different optical pump powers (see Figure S3a). Here we observe normal mode splitting, which indicates optomechanical strong coupling ($2g_{om} > \kappa_{opt}, \Gamma$), in addition to a large visibility in OMIT dip, indicating high optomechanical cooperativity ($C_{om} > 1$). We can directly extract optomechanical cooperativity and confirm its linearity against optical pump power by fitting the OMIT data ($C_{om} \propto N_p \propto P_p$, see Figure S3b). Microwave-to-optical transduction spectroscopy is measured across a range of optical pump power in Figure S3(c). The optical mode splitting from S3(a) is also visible in the transduction spectra in S3(c), particularly as the emergence of a left branch at high powers. The right branch is obscured due to interference with the electro-optic effect. To accurately match this model to our data, note that we have to use $g_{em}/2\pi = 347$ Hz (see Figure S3d). This is close to the simulated coupling rate, $g_{em}/2\pi = 298$ Hz, where the discrepancy can be attributed to the difference between simulated and machined microwave cavity and the shift in material properties in cryogenic conditions. The theoretical model is based on a comprehensive state space model that describes piezoelectric EM, Brillouin OM, and Pockel EO interactions, laid out in the following section.

B. State space model

(This subsection closely follows the works of reference [3, 4].) The Hamiltonian describing the system is

$$H/\hbar = \omega_p a_p^\dagger a_p + \omega_s a_s^\dagger a_s + \Omega_m b^\dagger b + \Omega_\mu c^\dagger c + (g_{om,0} a_p a_s^\dagger b + g_{em} b^\dagger c + g_{eo} a^\dagger c + \text{H.c.}), \quad (\text{S19})$$

where ω_p (ω_s) is optical wavelength of pump (signal) mode, Ω_μ is microwave cavity resonance frequency, and c is annihilation operator for microwave cavity mode. In the rotating frame with $H_0/\hbar = \omega_p a_p^\dagger a_p + \omega_s a_s^\dagger a_s$, we obtain an effective Hamiltonian

$$H_{\text{eff}}/\hbar = \Delta_o a_s^\dagger a_s + \Omega_m b^\dagger b + \Omega_\mu c^\dagger c + (g_{om,0} a_p a_s^\dagger b + g_{em} b^\dagger c + g_{eo} a^\dagger c + \text{H.c.}), \quad (\text{S20})$$

where $\Delta_o = \omega_s - \omega_p$ is the detuning of optical signal frequency from optical pump. In the undepleted pump regime, we can linearize the Hamiltonian about a strong, coherent pump, giving the expression

$$H_{\text{eff}}/\hbar = \Delta_o a_s^\dagger a_s + \Omega_m b^\dagger b + \Omega_\mu c^\dagger c + (g_{om} a_s^\dagger b + g_{em} b^\dagger c + g_{eo} a^\dagger c + \text{H.c.}), \quad (\text{S21})$$

where $g_{\text{om}} = \sqrt{N_p}g_{\text{om},0}$, and N_p is the intracavity pump photon number. The Heisenberg equations of motion for this Hamiltonian and the input-output relation between the fields are given by the following equations:

$$\dot{\mathbf{a}}(t) = A\mathbf{a}(t) + B\mathbf{a}_{\text{in}}(t) \quad (\text{S22})$$

$$\mathbf{a}_{\text{out}}(t) = B^T\mathbf{a}(t) - \mathbf{a}_{\text{in}}(t) \quad (\text{S23})$$

$$\mathbf{a} = (a, c, b)^T \quad (\text{S24})$$

$$\mathbf{a}_{\text{in}} = (a_{\text{in}}, c_{\text{in}})^T \quad (\text{S25})$$

$$\mathbf{a}_{\text{out}} = (a_{\text{out}}, c_{\text{out}})^T \quad (\text{S26})$$

$$A = \begin{pmatrix} -i\Delta_o - \frac{\kappa_o}{2} & ig_{\text{eo}} & ig_{\text{om}} \\ ig_{\text{eo}} & -i\Omega_\mu - \frac{\kappa_\mu}{2} & ig_{\text{em}} \\ ig_{\text{om}} & ig_{\text{em}} & -i\Omega_m - \frac{\kappa_m}{2} \end{pmatrix} \quad (\text{S27})$$

$$B = \begin{pmatrix} \sqrt{\kappa_{o,c}} & 0 \\ 0 & \sqrt{\kappa_{\mu,c}} \\ 0 & 0 \end{pmatrix}, \quad (\text{S28})$$

where \mathbf{a} is a vector for resonator mode operators and $\mathbf{a}_{\text{in(out)}}$ is a vector of input (output) fields. This is a simplified state space model in which we only include ports that we care about – in/output coupling ports. There are additional internal decay channels in this process that are not included in our model as we are assuming zero noise input.

In the frequency domain, we can reduce the expressions into a scattering matrix,

$$\mathbf{a}_{\text{out}}(\omega) = S(\omega)\mathbf{a}_{\text{in}}(\omega) \quad (\text{S29})$$

$$S(\omega) = B^T(-i\omega I - A)^{-1}B - I. \quad (\text{S30})$$

Using this scattering matrix, we can obtain various features that we can expect from our system, including OMIT, microwave-to-optical transduction, and optical-to-microwave transduction. Here we mainly focus on the transduction spectrum ($\eta(\omega) = |S_{\text{oe}}(\omega)|^2 = |S_{\text{eo}}(\omega)|^2$).

$$\eta(\omega) = \frac{\kappa_{o,c}}{\kappa_o} \frac{\kappa_{\mu,c}}{\kappa_\mu} \left| \frac{\alpha(\omega)}{\beta(\omega)} \right|^2 \quad (\text{S31})$$

$$\alpha(\omega) = 2(-\sqrt{C_{\text{em}}C_{\text{om}}} + iC_{\text{eo}}(1 - \frac{i(\omega - \Omega_m)}{\Gamma/2})) \quad (\text{S32})$$

$$\begin{aligned} \beta(\omega) = & 2i\sqrt{C_{\text{em}}C_{\text{om}}C_{\text{eo}}} + C_{\text{em}}(1 - \frac{i(\omega - \Delta_o)}{\kappa_o/2}) + C_{\text{om}}(1 - \frac{i(\omega - \Omega_\mu)}{\kappa_\mu/2}) + C_{\text{eo}}(1 - \frac{i(\omega - \Omega_m)}{\Gamma/2}) \\ & + (1 - \frac{i(\omega - \Delta_o)}{\kappa_o/2})(1 - \frac{i(\omega - \Omega_\mu)}{\kappa_\mu/2})(1 - \frac{i(\omega - \Omega_m)}{\Gamma/2}). \end{aligned} \quad (\text{S33})$$

We observe peak conversion when the optical detuning, microwave mode, and the acoustic mode are in resonance. Measuring transduction at this resonant frequency ($\omega = \Delta_o = \Omega_\mu = \Omega_m$), we get

$$\eta = \frac{\kappa_{o,c}}{\kappa_o} \frac{\kappa_{\mu,c}}{\kappa_\mu} \frac{4(C_{\text{em}}C_{\text{om}} + C_{\text{eo}}^2)}{4C_{\text{em}}C_{\text{om}}C_{\text{eo}} + (C_{\text{em}} + C_{\text{om}} + C_{\text{eo}} + 1)^2}. \quad (\text{S34})$$

In the case of no electro-optic coupling, Equation S34 can be reduced into the expression for a typical electro-optomechanical transduction.

$$\eta = \frac{\kappa_{o,c}}{\kappa_o} \frac{\kappa_{\mu,c}}{\kappa_\mu} \frac{4C_{\text{em}}C_{\text{om}}}{(C_{\text{em}} + C_{\text{om}} + 1)^2} \quad (\text{S35})$$

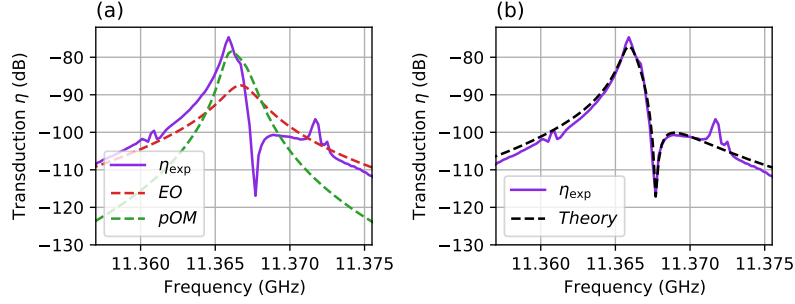


Fig. S4. Microwave to optical conversion measured (purple) is fitted using state space model. The data is taken at $P_p = 23.8$ mW. Separate OMIT measurement indicates $g_{\text{om}}/2\pi = 643$ kHz and $C_{\text{om}} = 1.48$. (a) Piezo-optomechanical (pOM) component (dashed green) and EO component (dashed red) of the fitted model is separately plotted against the conversion data. Fitted values of the coupling rates are $g_{\text{em}}/2\pi = 347$ Hz (theory value 298 Hz) and $g_{\text{eo}}/2\pi = 162$ Hz (theory value 137 Hz). (b) EO and pOM combined model (dashed black) fitted to data.

C. Presence of electro-optic (EO) effect in transduction spectrum

The expression of electro-optic (EO) coupling (Pockels effect) in materials is studied in various sources [5–8]. The single-photon electro-optic coupling rate between optical pump, optical signal, and microwave can be written as:

$$\begin{aligned} \hbar g_{\text{eo},0} &= \epsilon_0 \int_{\text{eo}} dV \epsilon_1 E_p \epsilon_1 E_s r_{13} E_\mu \\ &= \epsilon_0 \epsilon_1^2 r_{13} E_{p,0} E_{s,0} E_{\mu,0} \int_{\text{eo}} dV e^{-\frac{r^2}{2_{\text{opt}}}} e^{-\frac{r^2}{2_{\text{opt}}}} \sin(k_p z) \sin(k_s z), \end{aligned} \quad (\text{S36})$$

where r_{13} is the relevant linear electro-optic coefficient component. Electric fields of optical pump (E_p), optical signal (E_s) and microwave (E_μ) is defined as in the previous sections, with corresponding normalization factors of $E_{p,0} = \sqrt{2\hbar\omega_p/\epsilon_0\epsilon_1 A_{\text{opt}} L_{\text{opt}}}$ and $E_{s,0} = \sqrt{2\hbar\omega_s/\epsilon_0\epsilon_1 A_{\text{opt}} L_{\text{opt}}}$. $E_{\mu,0}$ is the zero-point electric field obtained through HFSS ($E_{\mu,0} = E_{\text{sim}}/2$), uniform along the interaction region. Assuming identical optical pump and signal mode profiles in both transverse and longitudinal direction, the above expression simplifies into,

$$g_{\text{eo},0} = \frac{1}{4} \epsilon_1 r_{13} E_{\text{sim}} \omega_p \frac{L_m}{L_{\text{opt}}}. \quad (\text{S37})$$

EO coefficient in quartz is $r_{13} = 0.45$ pm/V from crystal symmetry [9]. Resulting single photon EO coupling rate in quartz is $g_{\text{eo},0}/2\pi = 1.05$ mHz. Inside an optical cavity, this coupling rate is parametrically enhanced by the intercavity photon number ($g_{\text{eo}} = \sqrt{N_p} g_{\text{eo},0}$), reaching $g_{\text{eo}}/2\pi = 137$ Hz.

Incorporating a single-photon EO coupling rate into the state space model, we can compare our theoretical model to the transduction spectrum. In fact, we can even observe individual contributions from piezoelectric coupling and EO coupling to the net transduction. In Figure S4, transduction from piezoelectricity is in dashed green and that from EO is in dashed red. The combined net transduction is in dashed black can be fitted to the experimental data in purple, showing good agreement. Optomechanical coupling rate used in the fit is obtained through OMIT measurement ($g_{\text{om}}/2\pi = 643$ kHz and $C_{\text{om}} = 1.48$ at $P_p = 23.8$ mW). The fitted parameters are $g_{\text{em}}/2\pi = 347$ Hz (theory value is 298 Hz) and $g_{\text{eo}}/2\pi = 162$ Hz (theory value is 137 Hz). Such difference can be attributed to a discrepancy between the simulated microwave cavity and the assembled device, and to the variation in material parameters at cryogenic temperatures.

The apparent interference between piezoelectric and EO effect near the center peak is because of similar EM and EO cooperativities. In the relatively lossy acoustic cavity regime that we are operating, we can still reach $C_{\text{om}} > 1$. However, we have relatively low $C_{\text{em}} = 5.6 \times 10^{-8}$, which is greater than $C_{\text{eo}} = 2.8 \times 10^{-9}$ only by an order of magnitude. This is also observed in Figure S4, where the peak of theoretical EO transduction and that of theoretical pOM transduction are separated by 10 dB. As a result, we observe a fano interference in the transduction spectrum where the pOM response crosses through EO response. This destructive interference is visible

Suggested improvements	$g_{\text{em}}/2\pi$	C_{em}	$\eta_{\text{opt}}(\eta_{\mu})$	η
Current experiment	347 Hz	5.6×10^{-8}	0.53 (0.43)	1.2×10^{-8}
Optimized coupling efficiencies	-	-	~ 1 (~ 1)	$\uparrow 4\times$
X-cut quartz \rightarrow Z-cut LiNbO ₃	$\uparrow 7.3\times$	$\uparrow 50\times$	-	$\uparrow 50\times$
Optimized acoustic mode geometry	$\uparrow 9\times$	$\uparrow 80\times$	-	$\uparrow 80\times$
Re-entrant cavity	$\uparrow 3\times$	$\uparrow 10\times$	-	$\uparrow 10\times$
Superconducting cavity	-	$\uparrow 10^2\times$	-	$\uparrow 10^2\times$
Plano-convex hBAR	-	$\uparrow 10^3\times$	-	$\uparrow 10^3\times$
Combined improvement factors	$\uparrow \sim 200\times$	$\uparrow \sim 4 \cdot 10^9\times$	$\uparrow 2\times$ ($\uparrow 2\times$)	$\uparrow \sim 1.6 \cdot 10^{10}\times$
Combined improvement values	~ 68 kHz	~ 224	~ 1 (~ 1)	~ 0.9 ($C_{\text{om}} = C_{\text{em}} = 10$)

Table S1. Electromechanical cooperativity improvements

only on one side due to the phase relation between the pOM and EO interactions - constructive interference occurs on the other side.

One of the future paths to improve transduction, suggested in the manuscript, is using an acoustic cavity with better Q factor. Integration of a high-Q HBAR will bring about a significant increase in C_{em} , while keeping C_{eo} constant, thus suppressing the formation of such fano-like feature in future implementations of this design.

6. POTENTIAL IMPROVEMENTS IN TRANSDUCTION

Recall the transduction efficiency expression

$$\eta = \eta_{\text{opt}}\eta_{\mu} \frac{4C_{\text{om}}C_{\text{em}}}{(1 + C_{\text{om}} + C_{\text{em}})^2}. \quad (\text{S38})$$

In our system, we can readily reach C_{om} of 1 and $\eta_{\text{opt}}(\eta_{\mu})$ of 0.53 (0.43). Unity coupling efficiencies can be reached with ease by adjusting the microwave coupling pin to be over-coupled to the microwave cavity, and by having asymmetric optical cavity mirrors (i.e. creating a single-sided cavity). Also note that the Gaussian optical cavity mode is well-suited for achieving high fiber-coupling efficiency, a key challenge for low loss integration of a transducer. The expression therefore simplifies into

$$\begin{aligned} \eta &\approx C_{\text{em}} \\ &= \frac{4g_{\text{em}}^2}{\kappa_{\mu}\Gamma}, \end{aligned} \quad (\text{S39})$$

in the limit of small C_{em} ($C_{\text{em}} \ll C_{\text{om}}$) and assuming unity coupling efficiencies ($\eta_{\text{opt}} \approx \eta_{\mu} \approx 1$). Thus, improving the transduction efficiency boils down to improving C_{em} up to and above unity.

Among the approaches that we can take to enhance C_{em} , one obvious choice is to achieve stronger g_{em} as it is quadratically related to C_{em} . Rearranging Equation S4 in the bulk piezoelectric limit,

$$g_{\text{em}} = E_0 d_{33} c_{33} \sqrt{\frac{2A_{\text{m}}}{\hbar \Omega_{\text{m}} \rho L_{\text{m}}}}. \quad (\text{S40})$$

As laid out in Table S1, one way we can improve g_{em} is through choosing a stronger piezoelectric material, such as LiNbO₃ or BaTiO₃, instead of quartz. In the case of Z-cut LiNbO₃, piezoelectric tensor component increases from $d_{33} = 2.3$ pm/V to $d_{33} = 16.2$ pm/V, and stiffness tensor component from $c_{33} = 86.6$ GPa to $c_{33} = 244$ GPa. Even taking into account the impact from the change in density ($\rho = 2650$ kg/m³ to $\rho = 4630$ kg/m³), Brillouin frequency ($\Omega_{\text{m}} = 11.4$ GHz to $\Omega_{\text{m}} = 21.0$ GHz), and E_0 ($\frac{0.80}{\sqrt{2}} \times 10^{-3}$ V/m to $\frac{0.53}{\sqrt{2}} \times 10^{-3}$ V/m) due to higher relative permittivity, we can expect a higher g_{em} (C_{em}) by $7.3\times$ ($50\times$).

Another factor that influences g_{em} is the acoustic mode geometry. Increasing the acoustic mode waist allows us to achieve better mode matching between acoustic and microwave modes, while

thinner substrate thickness allows for lower mass acoustic mode (with larger zero point motion) while maintaining same acoustic-microwave mode overlap. Reasonable modifications can be made to the acoustic waist from 50 μm to 200 μm and to the substrate thickness (L_m) from 500 μm to 100 μm . This result in a higher g_{em} (C_{em}) by $9 \times (80 \times)$. Note that reducing the substrate thickness will decrease the g_{om} , yet it will not deter our ability to exceed unity optomechanical cooperativity ($C_{\text{om}} > 1$) as the current setup reaches $C_{\text{om}} \sim 10$ with relative ease.

Similarly, we can also improve the microwave and acoustic mode-matching by making modifications to the microwave cavity. In doing so, we will be optimizing E_0 , the remaining term in g_{em} . In order to reduce the microwave mode volume and concentrate the electric field, we can explore using a smaller coaxial microwave cavity or different cavity geometries such as a re-entrant cavity and other 2-D designs. Simulating a re-entrant cavity, we obtain approximately $3 \times$ stronger electric field compared to the coaxial design ($\frac{0.53}{\sqrt{2}} \times 10^{-3} \text{ V/m} \rightarrow \frac{1.8}{\sqrt{2}} \times 10^{-3} \text{ V/m}$), resulting in a higher g_{em} (C_{em}) by $3 \times (10 \times)$.

Besides optimizing g_{em} , we can also improve on other factors in C_{em} ; namely, κ_μ and Γ . This demonstration uses a non-superconducting cooper microwave cavity, with a modest $Q < 10^3$. With superconducting materials, both post and re-entrant cavities can readily reach $Q > 10^8$. Hence, in an ideal circumstance, κ_μ can be boosted by $> 10^5 \times$. However, we have to consider practical limitations such as the combination of high laser powers with superconducting resonators and the restriction in the bandwidth of the device that high Q microwave cavity may impose. In reality, we will consider a conservative enhancement in κ_μ by $> 10^2 \times$ as shown in Table S1. Diffractive loss in the acoustic cavity can be mitigated via shaping a concave surface on one side of the cavity through reactive-ion-etching. Doing so will allow the acoustic cavity to form stable resonances with Q up to $\sim 2.8 \times 10^7$ [10] from the current 2.3×10^4 , allowing us a $\times 10^3$ improvement in Γ at a cost in transduction bandwidth.

7. UNDERSTANDING CAF₂ DATA

Experimental parameters for CaF₂ are as following: detector resolution bandwidth 1 kHz, $\Omega_m = 13.354 \text{ GHz}$, $\Gamma = 535 \text{ kHz}$, $L_m = 0.5 \text{ mm}$, $A_m = 2\pi \times (64 \mu\text{m})^2$, $\kappa_o = 2.1 \text{ MHz}$, $\kappa_{o,c} = 0.598 \text{ MHz}$, $E_0 = 5.1 \times 10^{-4} \text{ V/m}$, $\kappa_\mu = 22.4 \text{ MHz}$, $\kappa_{\mu,c} = 10.9 \text{ MHz}$. For microwave driven motion measurement: $P_p = 23 \text{ mW}$, $g_{\text{om}} = 385 \text{ kHz}$, $C_{\text{om}} = 0.705$. For thermal phonon measurement: $P_p = 30.1 \text{ mW}$, $g_{\text{om}} = 427 \text{ kHz}$, $C_{\text{om}} = 0.914$.

Conversion from detected signal power to phonon number is done following the expression, $P_{\text{sig}} = (\hbar\omega_p)(\frac{4g_{\text{om}}^2}{\kappa_o\Gamma})\Gamma n_m$, where n_m is the number of driven phonons. In order to obtain piezo-electric coupling rate from the number of piezoelectrically driven phonons, we revisit the state space model for the equation of motion regarding electromechanical interaction with simplifications ($g_{\text{eo}} = g_{\text{om}} = 0$ and $\Delta_\mu = \Delta_m = 0$ where Δ_μ and Δ_m are detunings from microwave and mechanical resonance frequencies.),

$$\begin{aligned}\dot{c} &= ig_{\text{em}}b - \frac{\kappa_\mu}{2}c - \sqrt{\kappa_{\mu,c}}c_{\text{in}} \\ \dot{b} &= ig_{\text{em}}c - \frac{\Gamma}{2}b.\end{aligned}\tag{S41}$$

Assuming steady state, number of piezoelectrically generated phonons can be expressed as

$$n_m = \frac{4\kappa_{\mu,c}}{\kappa_\mu^2} \left(\frac{g_{\text{em}}}{\frac{2g_{\text{em}}^2}{\kappa_\mu} + \frac{\Gamma}{2}} \right)^2 \langle c_{\text{in}}^\dagger c_{\text{in}} \rangle,\tag{S42}$$

where $\langle c_{\text{in}}^\dagger c_{\text{in}} \rangle$ denotes the input microwave drive flux ($\langle c_{\text{in}}^\dagger c_{\text{in}} \rangle = P_\mu / \hbar\Omega_\mu$) and P_μ is the input microwave drive power. Considering the regime we are in ($\frac{2g_{\text{em}}^2}{\kappa_\mu} \ll \frac{\Gamma}{2}$), above expression simplifies to

$$n_m = \frac{4\kappa_{\mu,c}}{\kappa_\mu^2} \left(\frac{2g_{\text{em}}}{\Gamma} \right)^2 \langle c_{\text{in}}^\dagger c_{\text{in}} \rangle.\tag{S43}$$

In the experiment, P_μ , measured with a spectrum analyzer, is swept from 4 dBm to 20dBm. From Equation S43, we obtain electromechanical coupling rate, which turns out to be $g_{\text{em}}/2\pi = 0.03 \text{ Hz}$. Combining this with Equation S4, we can correlate a bulk piezoelectric constant of 0.083 fm/V or a surface piezoelectric constant of 2.44 pm/V across a 1 nm thick piezoelectric layer.

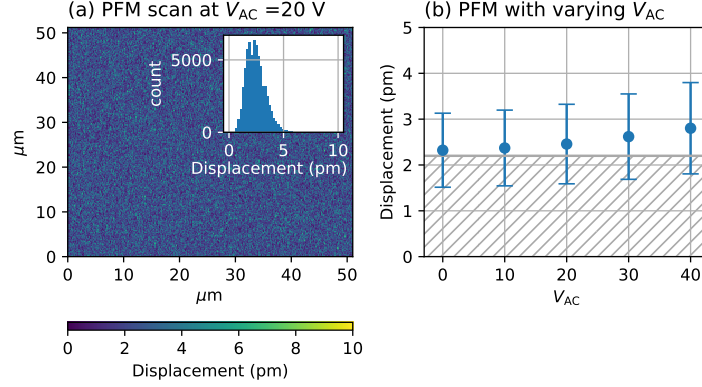


Fig. S5. PFM scan across a $50\text{ }\mu\text{m} \times 50\text{ }\mu\text{m}$ surface of CaF_2 . CaF_2 used here is the same substrate used in section 5 of the main text. (a) Example measurement at $V_{\text{AC}} = 20\text{ V}$. Histogram is shown in inset. (b) The average of displacement data is plotted with its standard deviation at various V_{AC} . Displacement noise floor of $\sim 2.2\text{ pm}$ is indicated in dashed grey. Minimal variability in detected displacement indicates piezoelectricity smaller than the device’s detection sensitivity.

8. ALTERNATIVE PIEZOELECTRICITY MEASUREMENT: PIEZORESPONSE FORCE MICROSCOPY (PFM)

Piezoresponse Force Microscopy (PFM) is a method of detecting piezoelectricity in $\sim 100\text{ nm}$ depth[11–13]. The substrate is put under an AC electric field (usually in the range of $\sim 100\text{ kHz}$), which leads to a piezoelectric deformation due to the converse piezoelectric effect. This deformation is mapped with a probe cantilever across the substrate. Recently an interferometric displacement sensing approach to PFM (IDS-PFM) has been developed which allows quantitative determination of out of plane electromechanical responses[12, 13]. This method removes many of the artifacts that plagues traditional PFM, and is made inherently quantitative via the interferometric read out.

We put the same CaF_2 that we study in section 5 of the main text under a IDS-PFM as a way to alternatively detect piezoelectricity (see Figure S5). The frequency of the AC field is $\sim 100\text{ kHz}$. We measure a white noise floor of $\sim 70\text{ fm}/\sqrt{\text{Hz}}$, which is equivalent to a displacement noise floor of $\sim 2.2\text{ pm}$ in an imaging bandwidth of 1 kHz . For a 1 V drive amplitude, this yields a minimum detectable piezo-sensitivity of $d_{\text{eff}} = 2.2\text{ pm/V}$. Minimum detectable piezo-sensitivity can be lowered by simply applying a larger drive voltage which was allowable in the case of CaF_2 , unlike thin films or materials having low dielectric breakdown potentials. For maximum applied voltage of 40 V , this implies a minimal detectable d_{eff} of 55 fm/V . From data, we barely see any deviation from the $\sim 2.2\text{ pm}$ background. Even though the data may appear to have a non-zero slope ($14 \pm 40\text{ fm/V}$), it is inconclusive that we detect any piezoelectricity since all data are within the standard deviation/error bar. We attribute the smaller but finite slope of 14 fm/V to influence of electrostatic forces. At high voltage especially, we can expect non-negligible electrostatic forces and force gradients to act between the AFM tip and sample, which may lead to small but finite displacement of the tip position, even for the case of IDS-PFM (which is largely insensitive to cantilever-sample electrostatic effects[12, 13]). We further note that using softer (3 nN) cantilevers than the one used in Figure S5 ($\sim 42\text{ nN}$) leads to a clear enlargement of the measured displacement (slope of $290 \pm 80\text{ fm/V}$) as would be expected for an electrostatic effect.

Therefore, we observe no detectable piezoelectricity though IDS-PFM, meaning that parasitic piezoelectricity in CaF_2 is smaller than the detection limit of 55 fm/V . These results indicate the unlikely-hood of the parasitic piezoelectricity coming from an intrinsic surface layer, which requires piezoelectricity to be $\gtrsim 1\text{ pm/V}$. Instead, it is more likely that the paracitic piezoelectricity detected in CaF_2 is originated from the bulk of the crystal.

REFERENCES

1. P. Kharel, G. I. Harris, E. A. Kittlaus, W. H. Renninger, N. T. Otterstrom, J. G. E. Harris, and P. T. Rakich, “High-frequency cavity optomechanics using bulk acoustic phonons,” *Sci. Adv.* **5**, eaav0582 (2019).

2. W. H. Renninger, P. Kharel, R. O. Behunin, and P. T. Rakich, "Bulk crystalline optomechanics," *Nat. Phys.* **14**, 601–607 (2018).
3. R. W. Andrews, R. W. Peterson, T. P. Purdy, K. Cicak, R. W. Simmonds, C. A. Regal, and K. W. Lehnert, "Bidirectional and efficient conversion between microwave and optical light," *Nat. Phys.* **10**, 321–326 (2014).
4. X. Han, W. Fu, C. Zhong, C.-L. Zou, Y. Xu, A. A. Sayem, M. Xu, S. Wang, R. Cheng, L. Jiang, and H. X. Tang, "Cavity piezo-mechanics for superconducting-nanophotonic quantum interface," *Nat. Commun.* **11**, 3237 (2020).
5. V. S. Ilchenko, A. A. Savchenkov, A. B. Matsko, and L. Maleki, "Whispering-gallery-mode electro-optic modulator and photonic microwave receiver," *JOSA B* **20**, 333–342 (2003).
6. A. Rueda, F. Sedlmeir, M. C. Collodo, U. Vogl, B. Stiller, G. Schunk, D. V. Strekalov, C. Marquardt, J. M. Fink, O. Painter, G. Leuchs, and H. G. L. Schwefel, "Efficient microwave to optical photon conversion: an electro-optical realization," *Optica* **3**, 597–604 (2016).
7. J. Holzgrafe, N. Sinclair, N. Sinclair, D. Zhu, D. Zhu, A. Shams-Ansari, M. Colangelo, Y. Hu, Y. Hu, M. Zhang, M. Zhang, K. K. Berggren, and M. Lončar, "Cavity electro-optics in thin-film lithium niobate for efficient microwave-to-optical transduction," *Optica* **7**, 1714–1720 (2020).
8. T. P. McKenna, T. P. McKenna, J. D. Witmer, J. D. Witmer, R. N. Patel, W. Jiang, R. V. Laer, P. Arrangoiz-Arriola, E. A. Wollack, J. F. Herrmann, and A. H. Safavi-Naeini, "Cryogenic microwave-to-optical conversion using a triply resonant lithium-niobate-on-sapphire transducer," *Optica* **7**, 1737–1745 (2020).
9. V. Ivanov, "Direct electro-optic effect in langasites and α -quartz," *Opt. Mater.* **79**, 1–7 (2018).
10. P. Kharel, Y. Chu, M. Power, W. H. Renninger, R. J. Schoelkopf, and P. T. Rakich, "Ultra-high-Q phononic resonators on-chip at cryogenic temperatures," *APL Photonics* **3**, 066101 (2018).
11. K. P. Kelley, D. E. Yilmaz, L. Collins, Y. Sharma, H. N. Lee, D. Akbarian, A. C. T. van Duin, P. Ganesh, and R. K. Vasudevan, "Thickness and strain dependence of piezoelectric coefficient in BaTiO₃ thin films," *Phys. Rev. Mater.* **4**, 024407 (2020).
12. L. Collins, Y. Liu, O. S. Ovchinnikova, and R. Proksch, "Quantitative Electromechanical Atomic Force Microscopy," *ACS Nano* **13**, 8055–8066 (2019).
13. A. Labuda and R. Proksch, "Quantitative measurements of electromechanical response with a combined optical beam and interferometric atomic force microscope," *Appl. Phys. Lett.* **106**, 253103 (2015).